MICROBIOLOGY

Negative feedback increases information transmission, enabling bacteria to discriminate sublethal antibiotic concentrations

Raul Ruiz, Fernando de la Cruz, Raul Fernandez-Lopez*

In the cell, noise constrains information transmission through signaling pathways and regulatory networks. There is growing evidence that the channel capacity of cellular pathways is limited to a few bits, questioning whether cells quantify external stimuli or rely on threshold detection and binary on/off decisions. Here, using fluorescence microscopy and information theory, we analyzed the ability of the transcriptional regulator TetR to sense and quantify the antibiotic tetracycline. The results showed that noise filtering by negative feedback increased information transmission up to 2 bits, generating a graded response able to discriminate different antibiotic concentrations. This response matched the antibiotic subinhibitory selection window, suggesting that information transmission through TetR is optimized to quantify sublethal antibiotic levels. Noise filtering by negative feedback may thus boost the discriminative power of cellular sensors, enabling signal quantification.

INTRODUCTION

Environmental sensing is essential for cell survival, yet noise in signal reception and gene expression constrains the ability of signaling pathways to reliably convey information (1, 2). At the signal reception level, the stochastic nature of diffusion and binding imposes a limit on the ability of cell receptors to quantify the concentration of diffusible molecules (1, 3, 4). At the signal transduction level, gene expression noise generates fluctuations in the copy number of the RNAs and proteins responsible for transducing the signal (5). Signal transduction pathways are thus inherently noisy, and the ability of the cell to control its internal sensory machinery is itself limited (2).

Noisy pathways are subject to an upper limit on the amount of information they can transmit, a quantity known as the channel capacity. Determining the channel capacity of signaling pathways and regulatory networks is thus essential to evaluate the sensing ability and regulatory power of the cell (6). The amount of information encoded by a noisy channel can be quantified in terms of Shannon's mutual information (MI), and it is usually measured in bits. Recent experiments have shown that signaling pathways exhibit low MI, with channel capacities of approximately 1 bit (7–11). The physiological significance of these observations has been a matter of debate. Because 1 bit is the amount of information required for a binary switch, Cheong et al. (7) proposed that 1-bit information transmission reflected a decision-making process fundamentally limited to on/off responses. Under this interpretation, 1 bit is indicative of a sensor with two possible states, able to detect a signal but unable to quantify it. However, the same amount of information (1 bit) may be transmitted by a graded sensor suffering from an associated inference error (12). Hence, observing 1 bit does not necessarily imply a digital controller. The ultimate question is whether signal transduction mechanisms are accurate enough to quantify external signals or whether molecular noise is so pervasive that the cell has no chance but to rely on threshold detection and on/off responses (Fig. 1A) (13). Answering this question has been complicated by the entan-

gled nature of eukaryotic regulation (14). Here, we investigate information transmission by the prokaryotic transcriptional repressor TetR, a regulator of tetracycline (Tc) resistance, and a widely used workhorse for controlled gene expression in synthetic gene networks.

TetR is the prototype of a large family of one-component signal transduction systems involved in responses against small molecules, such as antibiotics, quorum-sensing molecules, and metabolites. TetR regulates the expression of TetA, a protein conferring Tc resistance. Expression of TetA is deleterious to the host cell; hence, its production is tightly regulated and only occurs when Tc is present in the environment (15). Although the molecular mechanisms involved in TetR regulation have been thoroughly described (Fig. 1B), whether this prototypic circuit responds to the antibiotic in a graded fashion or as an all-or-none switch is currently unknown. Moreover, in recent years, it has become clear that subinhibitory antibiotic concentrations can exert selective pressure and elicit a variety of cellular responses (16). Determining what range of antibiotic concentrations is actively monitored by the cell, and with how much precision, might help us understand the overall impact of antibiotic pressure on microbial communities

Using fluorescence microscopy, single-cell analysis, and information theory, we measured information transmission in the TetR senso-regulatory circuit. We analyzed the influence of network architecture on information transmission and determined the overall ability of the system to quantify and respond to the signal (Tc). Our results show that TetR is able to convey up to 2 bits of information, being able to discriminate antibiotic levels below the minimal inhibitory concentration (MIC). In its natural setting, TetR engages in a negative feedback loop (NFL) that increases information transmission through the signaling pathway, enabling signal quantification.

RESULTS

TetR is a classical representative of one-component systems, the most prevalent pathways for signal transduction in prokaryotes (17). Like other one-component sensors, TetR has a dual role, acting simultaneously as a signal receptor (binding Tc) and as a signal transducer (regulating gene expression). TetR represses the expression of the

Instituto de Biomedicina y Biotecnologia (IBBTEC) CSIC/Universidad de Cantabria, Santander, Spain.
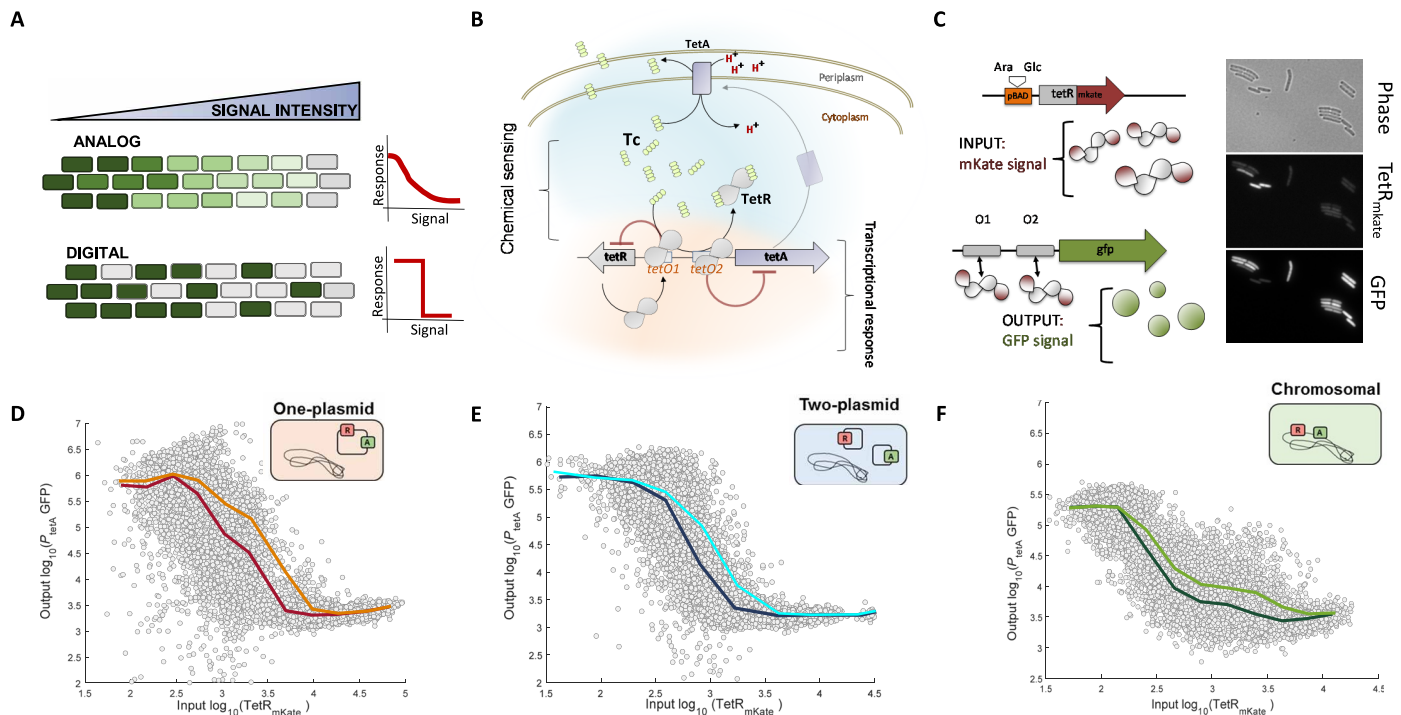*Corresponding author. Email: raul.fernandez@unican.es

Fig. 1. Structure of TetR/TetA circuit and experimental setup. (**A**) Scheme of analog (graded) and digital (on/off) responses against a signal. (**B**) Scheme of TetR/TetA circuit. (**C**) Experimental design (right) showing TetR$_{mkate2}$ fusion cloned under the transcriptional control of a regulatable pBAD promoter (INPUT) and GFP cloned under pA promoter (OUTPUT). Microphotographs show *Escherichia coli* cells carrying both reporters (left). Cells were grown on agarose pads, as described in Materials and Methods. Exposure times were 50 ms (phase) and 500 ms (mkate2 and GFP). (**D** to **F**) Each panel shows input (TetR$_{mkate2}$) versus output (GFP) fluorescence levels (fluorescence arbitrary units) for 9000 individual cells, corresponding to different genomic constructions: input and output cloned in the same plasmid (D), on two separate plasmids (E), and into the chromosome (F). Lighter solid lines indicate population averages, and darker solid lines correspond to median values.

Tc resistance protein TetA by binding two operators (*tetO1* and *tetO2*) located in the pA promoter (Fig. 1B). Upon binding to Tc, TetR suffers a conformational change that prevents recognition of its cognate operators. Thus, information about the signal (Tc) is conveyed to pA expression levels by the amount of inducer-free TetR. To quantify the MI between inducer-free TetR and pA expression levels, we needed the output conditional distribution $P(\text{pA}|\text{TetR})$, that is, the distribution of pA expression levels produced in response to a gradient of inducer-free TetR. For this purpose, we generated a translational fusion between TetR and the red fluorescent protein mKate2, and a transcriptional fusion between pA and the green fluorescent protein (GFP) (Fig. 1C). This way, we could simultaneously monitor, in single cells, input TetR$_{mkate2}$ and output pA::GFP levels (Fig. 1C).

TetR$_{mkate2}$ is functional and does not increase noise in the signaling pathway

The translational fusion TetR$_{mkate2}$ was fully functional and able to repress transcription from the pA promoter (fig. S2). The functionality of the FP fusion, however, did not guarantee a physiological behavior of the protein, because FP fusions are known to cause distribution artifacts. As shown by Landgraf *et al.* (*18*), FPs are "sticky" and may induce the formation of transitory aggregates when fused to other proteins. These aggregates are often functional, yet they decrease the effective number of protein particles that binomially partition between daughter cells during cell division. This increases the segregation error and the noise experienced by downstream pro-

cesses (*18*). Because information transmission is hampered by noise, this effect may result in an overall reduction in the observed channel capacity. To check for this possibility, we performed a fluctuation after cell division test (*18*). Briefly, this test consists in measuring the fluctuations exhibited by daughter cells, immediately after cell division, in a downstream process affected by the FP fusion (fig. S2). In our case, we compared the fluorescence produced by pA::GFP between daughter cells. We compared the results between strains that contained TetR$_{mkate2}$ (RRG112) and cells containing *wt* TetR (RRG28). As shown in fig. S2, we did not detect any substantial increase in pA::GFP fluctuations due to the mKate2 fusion. We concluded, therefore, that the translational fusion was functional and did not cause any apparent increase in the overall noise levels of the signaling pathway.

Measuring MI between TetR$_{mkate2}$ and pA

Measuring the MI between TetR$_{mkate2}$ and its target promoter pA required sampling pA responses against the widest possible range of TetR$_{mkate2}$ inputs (*19*). To this end, we cloned *tetR$_{mkate2}$* under the control of the inducible promoter pBAD (Fig. 1) (*20*). This allowed us to generate a continuous input gradient, which spanned approximately 100-fold (figs. S3 and S4). To determine whether the plasmidic or chromosomal location of the circuit had any effect on information transmission, we cloned our experimental system in three different genomic settings (Fig. 1, D to F). Because plasmid copy number is also subject to random fluctuations (*21*), these different genomic settings allowed us to determine the impact of different noise regimes
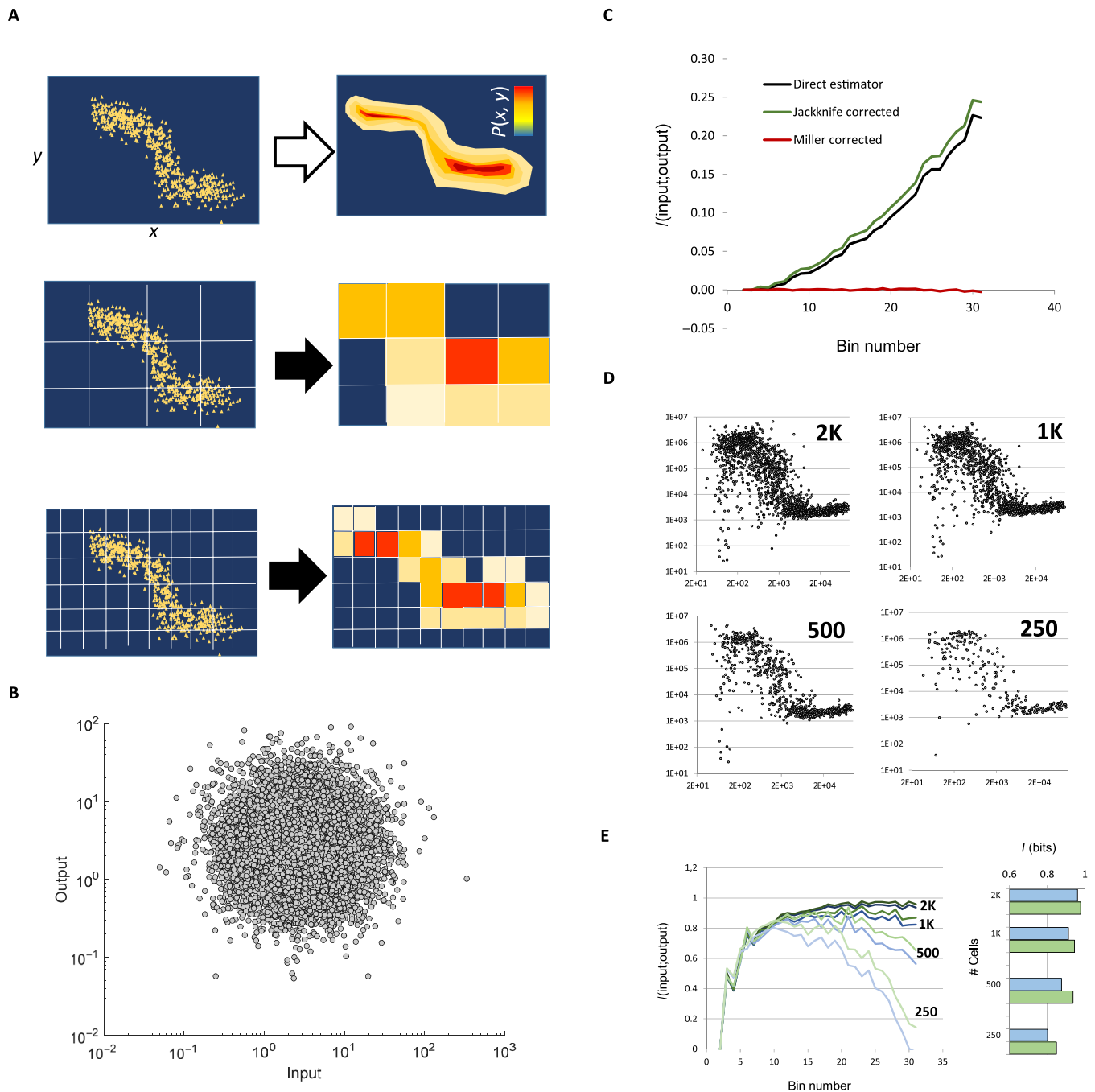
Fig. 2. Extracting MI values from scatterplot data. Measuring entropy and MI from scatterplot data. (**A**) To measure MI, scatterplot data showing input and output values (upper left panel) must be transformed into a two-dimensional probability density plot (upper right panel). To do so, we used Grenander's method of sieves, as discussed in Supplementary Results. The middle and bottom panels of the figure show the application of two sieves of different bin sizes. The middle panel shows a sieve with a low number of bins, while the bottom panel shows a sieve with a high number of bins. On the right of the figure, the probability density maps result from applying different sieves on the same scatterplot map. (**B**) Scatterplot of 9000, log-distributed, random input/output pairs used to test the performance of discretization methods. Because this dataset was randomly generated, discretization should result into 0 bits of MI. (**C**) MI values extracted from scatterplots from (B) using the discretization methods indicated in the figure. Blue, direct H_{ML} estimation; green, direct H_{ML} estimation under jackknife correction; red, H_{CML} estimation (maximum likelihood with Miller's correction). As shown in the figure, Miller's correction was required to prevent information inflation due to increasing bin number. (**D**) Datasets of different sizes generated to test the effect of undersampling on MI estimation. From the experimental dataset shown in Fig. 1D, we randomly drew 2000, 1000, 500, and 250 cells, generating the four datasets shown in the figure. (**E**) Effect of sampling size on MI estimation with and without jackknife correction. On the left panel, lines indicate the MI estimation for different bin sizes (x axis), retrieved when applying H_{CML} estimation with (green lines) and without (blue lines) jackknife correction. On the right panel, MI estimations for datasets shown in (D) with (green bars) and without (blue bars) jackknife correction. As detailed in Supplementary Results, jackknife correction provided only a marginal improvement of less than 1% of the MI.

on TetR (fig. S5). A gradient of TetR$_{mkate2}$ concentrations was then generated by differentially inducing pBAD, and input and output levels were measured by fluorescence microscopy (Fig. 1, D to F).

Determining MI between TetR$_{mkate2}$ and pA also required transforming input/output scatterplots into probability density maps [P(input,output)]. For that purpose, a mesh of variable size was applied to bin experimental data (Fig. 2A). Probabilities were then obtained using a maximum likelihood estimator (H_{ML}) (*22, 23*). As shown in Fig. 2A, decreasing the bin size should, in theory, improve our estimation of P(input,output). However, this procedure is known to artificially inflate MI as the number of bins is increased. To avoid this problem, we introduced Miller's correction in our maximum likelihood estimator (H_{CML}) (*22, 23*). We checked that this procedure prevented artifactual MI inflation by applying it to a random distribution with a domain equivalent to that of our experimental results (Fig. 2B). This random distribution should show 0 bits of MI, but direct H_{ML} estimation generated MI inflation (Fig. 2C). In contrast, H_{CML} correction prevented this problem, yielding the expected MI. When applied to experimental data, H_{CML} approaches an asymptotic maximum that is taken as the true MI (Fig. 2E) (*9*). As described by Hansen and O'Shea (*9*), the error in MI estimation

can be obtained from the SD of MI values in the asymptotic region. All our MI measurements showed SDs between 0.01 and 0.03 bits. Another common problem in determining MI from experimental data arises from undersampling, which reduces our ability to correctly assign probabilities to each bin. Jackknife resampling can be used to correct for this problem (*7, 9, 23*). However, our experimental sample sizes (>2000 cells in all cases) were well beyond the undersampled regime (Fig. 2D). A complete description of the methods used for MI estimation can be found in Supplementary Results.

Input/output scatterplots were transformed into probability density maps, and from these maps, MI values were obtained as described before. The results showed MI values close to 1 bit, regardless of genomic location (Fig. 3, A to C). Because the input distribution obtained from pBAD was not uniform across the overall induction range, we analyzed the output distribution (pA::GFP levels) under equiprobable inputs. For this purpose, from the datasets shown in Fig. 1 (D to F), we computationally generated uniform TetR$_{mkate2}$ distributions (Fig. 3, D to F). The resulting MI under equiprobable inputs (MI$_U$) yielded 0.980 ± 0.02 bits for the one-plasmid system (RRS113), 1.06 ± 0.01 bits for the two-plasmid system (RRS112), and 0.88 ± 0.01 bits for the chromosomal insertion (RRS247). Thus,
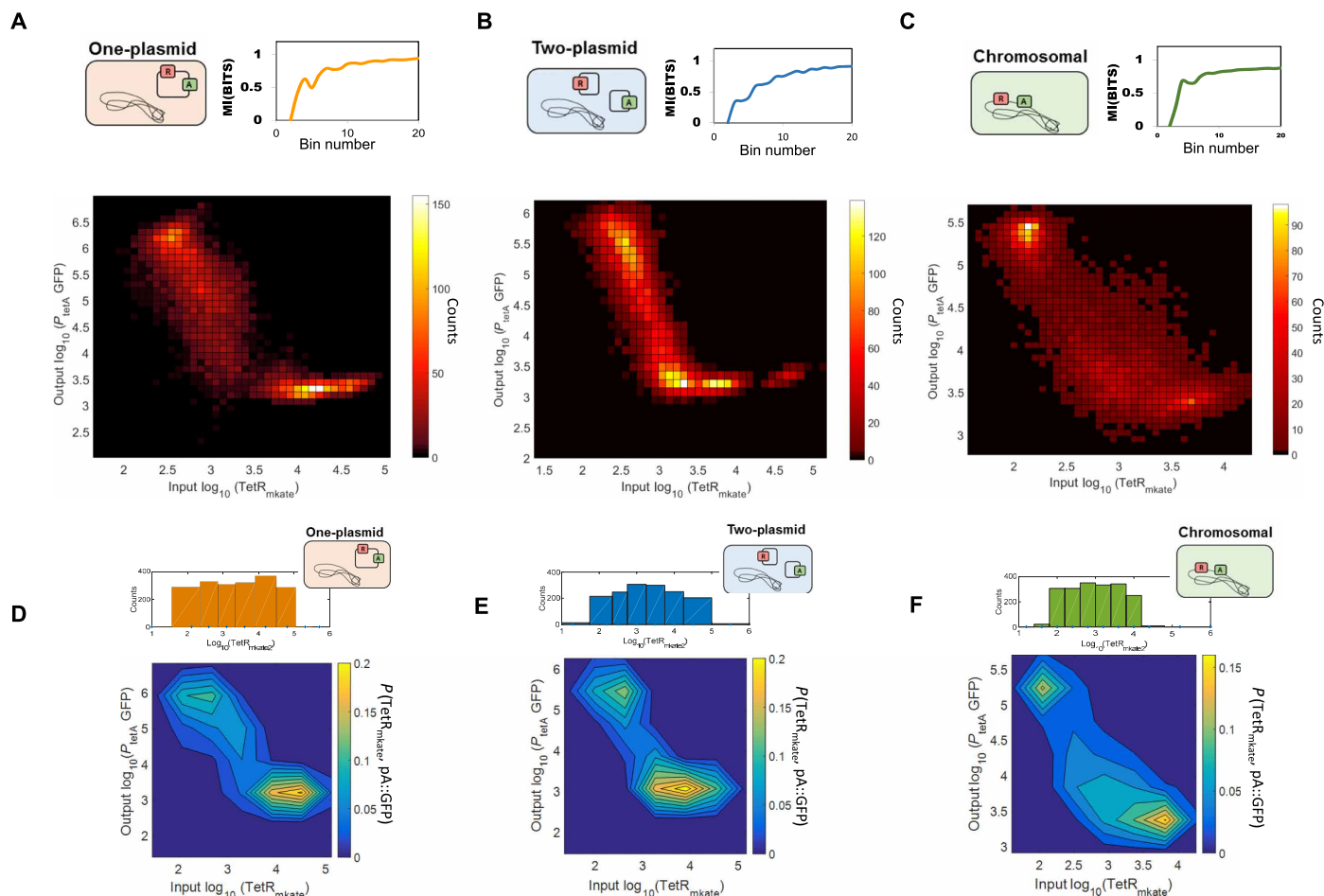

Fig. 3. Determining the MI between TetR$_{mkate2}$ and pA. (**A** to **C**) MI values (top) and density maps (bottom) for the different genomic constructions. Input/output scatterplots were transformed into density plots by applying a mesh of variable bin sizes, as described in the main text. Upper chart shows MI values (*y* axis) as a function of the number of bins (*x* axis). Asymptotic MI values were taken as the lower bound of the MI. Density maps correspond to bin sizes yielding maximum MI. (**D** to **F**) Probability density maps for equiprobable inputs. Upper charts shows TetR$_{mkate}$ input distributions. Lower charts show joint probability density maps P(TetR$_{mkate}$, pA::GFP). Probability densities follow the color bars on the right.

the results indicated that overall MI_U levels were similar for the three genomic locations (Fig. 3, D to F). It is noteworthy, however, that the chromosomal construction displayed slightly lower MI_U, despite showing lower output noise levels (fig. S5). This can be explained by the smaller $TetR_{mkate2}$ induction range exhibited by this construction (compare x axis in Fig. 3). This difference in induction ranges is most likely due to the higher copy number achieved by plasmid constructions (which contain pSC101 replication origins) compared to the chromosome (21).

Once we obtained P(input, output) density maps, we could assess whether pA responses corresponded to an on/off binary switch or, alternatively, to an analogic sensor able to quantify the signal. Judging from MI_U values and the probability density maps shown in Fig. 3, the answer was actually neither. Despite conveying 1-bit MI, the response could not be characterized as a pure on/off switch, because intermediate $TetR_{mkate2}$ concentrations generated intermediate pA levels. These intermediate values, however, were so noisy that the ability of the sensor to quantify the signal was severely compromised. Just moving 15% away from the on/off saturating pA values, MI_U levels in RRS113 dropped from 1.06 ± 0.01 bits to 0.28 ± 0.03 bits. Thus, the results indicated that the TetR/pA circuit could not be categorized as a strict digital switch or an effective analogic sensor.

Measuring MI between Tc, $TetR_{mkate2}$, and pA

A gradient of TetR, artificially induced from the pBAD promoter, was able to convey 1 bit of information to its target promoter. Total TetR concentration, however, is not the natural input of the TetR/TetA circuit. Rather, the inducer of the system, Tc, binds TetR, inactivating it and preventing repression of pA. Therefore, in its natural setting, pA responds to changes in the levels of free TetR rather than to changes in its total concentration. Although the same TetR gradient can be generated by Tc inactivation or by TetR synthesis/degradation, theory predicted that each of these mechanisms would exhibit different noise levels (Supplementary Calculations). Noise constrains information transmission (2); thus, MI values may depend on the way the input gradient is generated. To test this possibility, we measured MI_U between Tc (input) and pA::GFP (output). To this end, $TetR_{mkate2}$ was induced to saturating levels in RRS113 cells. These cells were then subjected to a Tc gradient, imaged, and analyzed as described in Materials and Methods. From the (Tc, pA::GFP) scatterplot (Fig. 4A), we obtained the P(input,output) density map (Fig. 4B). In this case (and in all experiments using Tc), the number of input bins was fixed to the number of Tc induction levels. Output GFP levels were analyzed at variable binning, as described previously. The results demonstrated overall lower output noise levels (Fig. 5A) and a MI_U value of 1.54 ± 0.02 bits. This latter value represented a 60% increase in the amount of information transmitted by a uniform Tc gradient compared to the uniform $TetR_{mkate2}$ gradient generated by arabinose induction. The output distribution showed a clear mode for the OFF state, but ON levels displayed a broader distribution, with one major peak and several local maxima (Fig. 4C). Overall, the results showed that Tc induction generated lower output noise levels, increasing information transmission.

A negative feedback on TetR increases information transmission

Tc induction generated lower pA output noise levels, yielding higher MI values. These findings motivated us to study the influence of network architecture, a well-known factor determining noise prop-

agation in transcriptional circuits (10). At its native location in the Tn10 transposon, TetR is transcribed from pR, a promoter overlapping pA and oriented in the opposite direction (Fig. 4E). Expression from pR is repressed by TetR; thus, TetR engages in an NFL. This NFL implies that the effect of Tc on the circuit is twofold. On the one hand, Tc decreases the levels of free TetR, thus reducing its ability to repress pA transcription. On the other hand, lower levels of free TetR also increase pR transcription, increasing total TetR concentration. To analyze the overall impact of this NFL on the ability of TetR to discriminate Tc, we built the experimental system shown in Fig. 4E. In this construction, $TetR_{mkate2}$ was cloned under its cognate promoter pR, while GFP remained under the control of pA. E. coli cells carrying this construct (RRS129) were subjected to a gradient of Tc concentrations, and output pA::GFP levels were measured by fluorescence microscopy, as described in Materials and Methods. Input/output scatterplots (Fig. 4, E and I) were transformed into P(input,output) density maps, as described before. The results demonstrated that, under the same Tc gradient, the NFL circuit yielded MI_U = 1.96 ± 0.01 bits, while the NFL-free circuit produced 1.54 ± 0.02 bits. This increase in information transmission was accompanied by a substantial decrease in output noise (Fig. 5A). Noise filtering is a well-known property of NFLs, and it has been shown that some degree of feedback tends to improve information transmission in signaling pathways (24, 25). However this noise-filtering power comes at the cost of reducing the system's sensitivity to the input (26). This trade-off between input sensitivity and noise suppression implies that the adaptive value of NFLs in signal reception cannot be taken for granted. To shed light on this question, we followed Tkačik et al. (24) and analyzed theoretically how information transmission in a sensory circuit depended on the presence of a negative feedback. This required assuming that the overall circuit behavior can be approximated by a Gaussian channel (10, 19, 24, 27). Although noise in bacterial transcription and translation is generally non-Gaussian, this approximation has provided insights in qualitative agreement with experimental results (10, 28). An analysis of the theoretical channel capacity of an ideal one-component sensory circuit, with and without feedback, is shown in Supplementary Calculations. The results revealed that a noncooperative negative feedback (n = 1) operating on the sensor (TetR, in this case) achieved higher channel capacities than its unregulated counterpart. Moreover, a noncooperative feedback was also observed to overperform NFLs displaying cooperativity ($n \geq 2$). Thus, theory predicted that a negative feedback on TetR, with n = 1, was optimal for MI transmission.

We then determined the apparent cooperativity of the NFL feedback operating on TetR. For this purpose, we measured the average responses of pR and pA promoters to Tc induction. The average response by pA showed a sigmoidal curve, with apparent cooperativity n = 2. In contrast, the response from pR was observed to be hyperbolic, with n = 1. Therefore, TetR engages in a noncooperative feedback, the strategy predicted by theory to yield the best MI transmission (Fig. 5B). The results shown in Fig. 5B were also in full accordance with previous in vitro data showing that (i) TetR affinity for tetO1 is 50% lower than for tetO2 and (ii) repression of pA requires binding to tetO1 and tetO2, while pR responds to tetO1 only (29).

TetR discriminates Tc concentrations in the subinhibitory range

Differences in information transmission and dynamic responses by pR and pA promoters translated into different sensing precision levels.
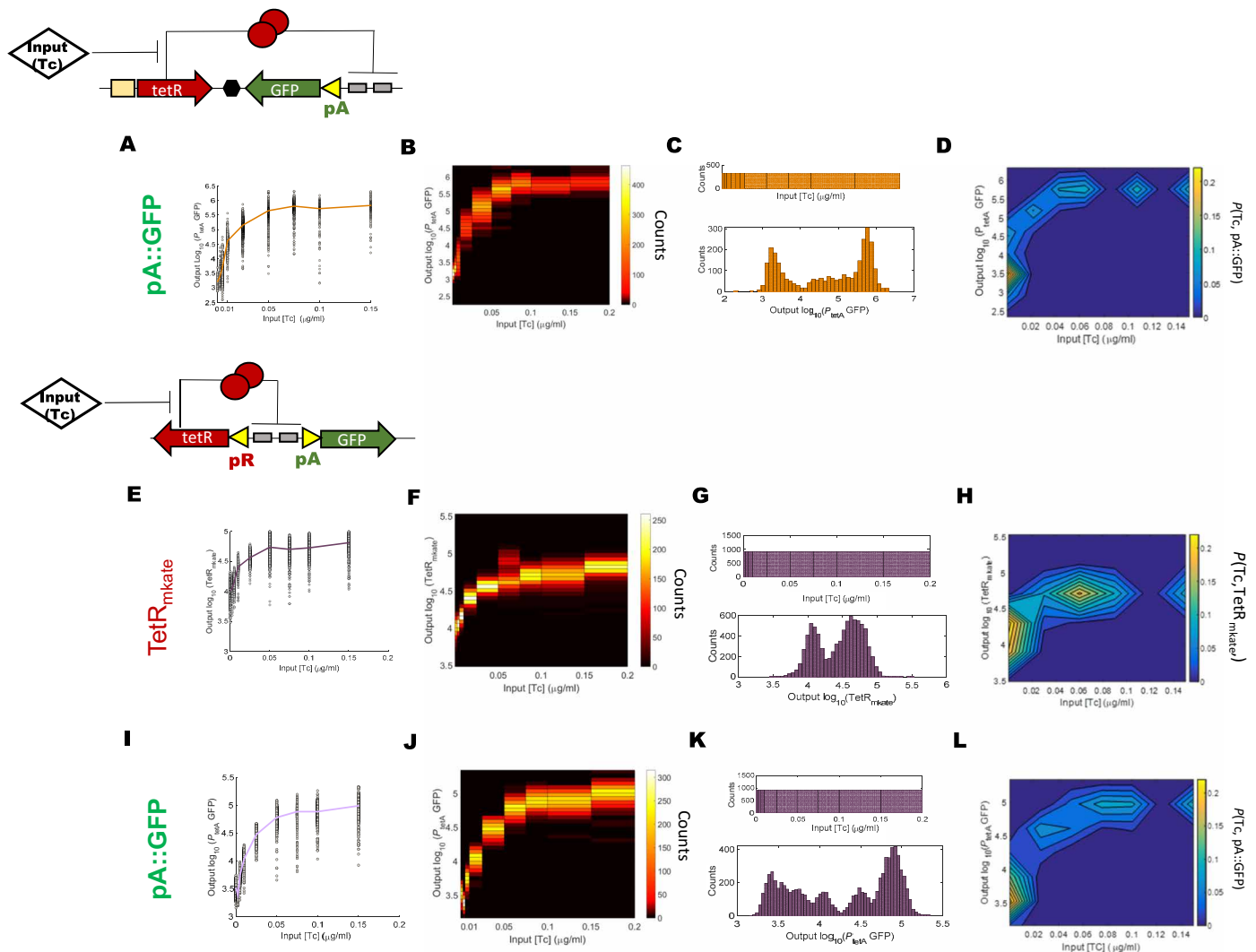
Fig. 4. Measuring information transmission by the inducer, Tc. (**A** to **D**) Data for one-plasmid experimental system without NFL. (**E** to **L**) Data for one-plasmid system under TetR NFL. From these, (E) to (H) show data from pR::TetR$_{mkate2}$ expression, while (I) to (L) correspond to pA::GFP values. (A, E, and I) Scatterplots showing fluorescence intensity (y axis, arbitrary fluorescence units) in response to increasing Tc concentrations (x axis, in μg/ml). Solid lines correspond to average values. (B, F, and J) Density maps obtained using optimal bin sizes, as described in the main text. (C, G, and K) Histogram of input (top) and output levels (bottom). Upper chart shows uniform distribution of input Tc concentrations. Lower chart shows the output fluorescence distribution produced from pR or pA promoters. (D, H, and L) Probability density maps for the joint input/output probability distributions. Probability densities are indicated according to the color bar.

TetR$_{mkate2}$ levels produced from pR could be divided into two regions (H1 and H2 in Fig. 5C), which discriminated between Tc concentrations above and below 0.01 μg/ml. Meanwhile, GFP levels produced from pA showed four discriminative quartiles, each one corresponding to a different Tc concentration range (Q1 to Q4 in Fig. 5C). Analysis of the impact of growing Tc concentrations on bacterial growth rates revealed a correlation between pA output levels and the antibiotic effect (Fig. 5E). Tc concentrations without detectable effects on bacterial growth did not elicit responses from pR/pA. Increasing concentrations above this threshold, however, pushed cells into higher pR/pA expression levels (Fig. 5D). The results demonstrated that the 2-bit MI displayed by the system allowed the discrimination of four Tc concentration ranges, corresponding to four different levels of antibiotic toxicity. Using rate-distortion methods, we used the conditional output distribution (Fig. 4K) to back-calculate the MI theoretical maximum (Supplementary Results). This theoretical

maximum corresponds to the channel capacity of the pathway. The results showed that the TetR/TetA circuit uses 90% of its channel capacity, the system being optimized to discriminate antibiotic concentrations well below the MIC, between 5 and 25 nM (Fig. 5F).

DISCUSSION

Information transmission through biochemical networks is essential for cell survival, yet experimental measurements have revealed channel capacities around 1 bit (7, 8, 12). While these values do not imply that cells necessarily rely on binary computation (12), they nevertheless represent low channel capacities, poorly suited for accurate signal quantification (30). Eukaryotes may solve this problem by using alternative signaling strategies, such as encoding information in transcription factor dynamics (8) or relying on collective decision-making (31). In bacteria, however, these strategies have not been
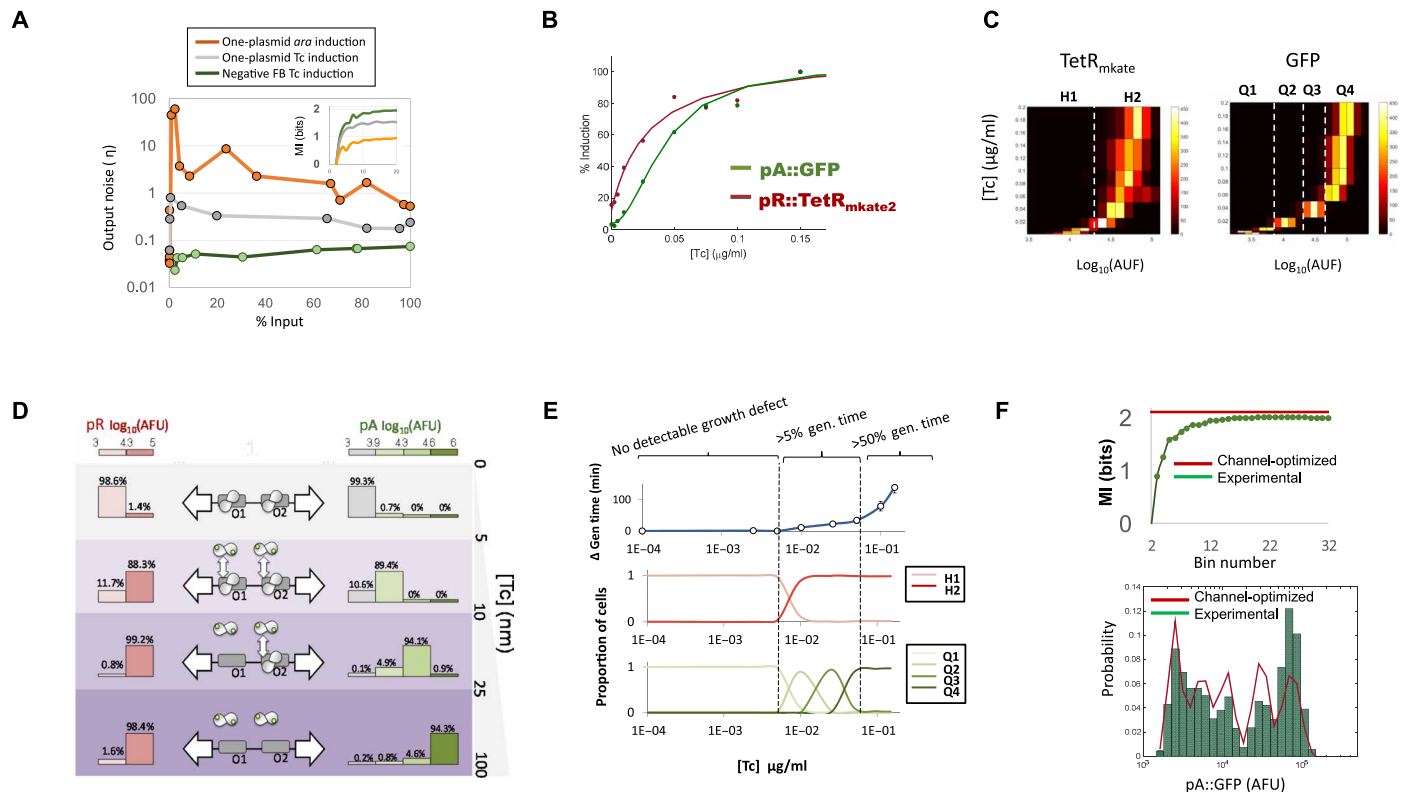
Fig. 5. Discrimination of sublethal antibiotic concentrations. (**A**) Output pA::GFP noise levels, expressed as variance divided by squared average achieved by the one-plasmid system. Values shown in the figure correspond to the circuit without feedback under arabinose or Tc induction (orange and gray lines, respectively) and to the circuit with NFL under Tc induction (green line) (inset: MI values observed in each experimental condition; x axis corresponds to the number of bins for the output). (**B**) Tc transfer function for pA::GFP (green line) and pR::TetR$_{mkate2}$ (red line) (y axis, promoter induction levels, expressed as % of the maximum; x axis, Tc concentration, in μg/ml). (**C**) Discriminative regions in pR/pA expression levels. White lines indicate boundaries between expression levels that unambiguously correspond to different Tc concentrations. (**D**) Model of pR/pA responses versus Tc concentration. Bars indicate percentage of cells located in each of the pR/pA regions, as Tc concentration increases (right). (**E**) Correlation between Tc effect and pR/pA activation levels. Upper chart shows increases in the doubling time (y axis, in minutes), plotted against Tc concentration (x axis, in μg/ml). Middle and lower charts show the percentage of cells showing values within pR and pA expression levels, respectively. (**F**) Channel capacity optimization. Top: Experimental MI values (green line) compared to the theoretical channel capacity (red line) calculated by rate-distortion methods. Bottom: Experimental output distribution (green bars) compared to optimal output distribution calculated by rate-distortion methods (red line).

described, and with a few remarkable exceptions (*25, 32, 33*), the information capabilities of prokaryotic signaling pathways remain largely unexplored. Signal transduction in prokaryotes is mostly undertaken by one-component response regulators, proteins able to bind to specific molecules and modify gene expression accordingly (*17*). Here, we analyzed the ability of TetR, a canonical one-component regulator, to convey information about its cognate inducer, the antibiotic Tc.

The results showed that the TetR response against Tc was neither intrinsically digital nor analog but was heavily conditioned by the noise levels experienced by the signaling pathway. Noise filtering by negative feedback was key for the system to achieve a channel capacity of 2 bits. While this channel capacity may not represent a marked increase over levels reported for other pathways, it was enough for the cell to discriminate between different antibiotic concentrations. The overall ability of TetR to quantify the signal may seem poor. However, one must take into consideration that sensors and transducing molecules are generally present at low copy numbers and that transcription factors are usually found in the nanomolar range. At these concentrations, noise is expected to severely constrain channel capacities, with upper limits predicted to be around 3 bits (*34*). While

it is possible for the cell to improve information transmission by increasing the concentration of sensors and transducing molecules, this strategy quickly leads to diminishing returns, demanding astronomic investments to boost signal detection (*2, 34*). It is thus likely that the sensing ability of TetR and other cellular sensors is primarily constrained by cellular economy. The results showed that an NFL increased information transmission in TetR. Similarly, theory indicated that a noncooperative NFL operating on the sensor optimizes the channel capacity of one-component response regulators. If economy is a critical factor limiting sensing precision, then the advantage of an NFL may be twofold. It not only increases information transmission but also reduces the sensor concentration at the steady state when the signal is not present. An NFL operating on the sensor may thus increase information transmission while simultaneously reducing the metabolic burden imposed by the sensory pathway.

One of the key features of information transmission through the TetR circuit was its ability to discriminate antibiotic concentrations below the MIC (Fig. 5D). Sub-MIC antibiotic levels may not kill bacteria, but this does not imply that they are innocuous. Subinhibitory antibiotic concentrations may damage the cell, decreasing the growth rate of susceptible populations (Fig. 5E). The sub-MIC selection

window comprises all antibiotic concentrations below the MIC that produce a fitness deficit big enough to promote the evolution of resistant strains (*16*). In *E. coli*, the minimal selective concentration for Tc was found to be 15 ng/ml (*35*). The minimal informative concentration in our experiments was 10 ng/ml. Thus, our results support the idea that TetR-mediated resistance is primarily aimed against sublethal antibiotic doses that directly impair cell growth. In the environment, antibiotics rarely achieve the concentrations used in the clinical setting, yet sub-MIC levels are frequent, as a result of widespread antibiotic contamination (*36*). Quantifying the signal also makes sense in the context of repeated exposure to subinhibitory levels of antibiotic. Concentrations over the MIC are lethal; thus, their effect on fitness is likely to be close to binary (dead/alive), depending on whether bacteria express resistance. In contrast, subinhibitory levels have an incremental effect on growth rates (Fig. 5E). Because TetA expression is known to be metabolically expensive (*15*), it may pay off for the cell to invest in a sensory system able to adjust resistance levels to the fitness deficit caused by different sub-MIC antibiotic concentrations. Testing this hypothesis is complicated by the need for precise methods to quantify the fitness distribution, in single cells, under sublethal antibiotic levels. If achievable, however, this analysis may shed light on the elusive relationship between the sensory power of the cell and its overall impact on cellular fitness.

MATERIALS AND METHODS

Bacterial strains
All bacterial strains used in this study were derivatives of *E. coli* K-12 and are listed in table S1.

Plasmid construction
Plasmid pRRG13 (fig. S1A, upper right side) was generated by inserting the *tetA* promoter region (pA) in front of the *gfp* gene in plasmid pUA66. Promoter pA was polymerase chain reaction (PCR) amplified from the Tn*10* region of the natural plasmid R100 using oligonucleotides pTetA1XhoI and pTetA2BamHI. The resulting band was inserted in pUA66 using Xho I and Bam HI restriction endonucleases. The TetR$_{mkate2}$ fusion protein was generated by binding the N terminus of protein mKate2 to the C-terminal end of TetR through a flexible linker made of Ser-Gly-Gly-Gly-Gly peptide. For this purpose, we constructed plasmid pRRG54. Plasmid pRRG54 was built by Gibson assembly out of three DNA fragments. The first one was the PCR product of amplifying *mkate2* with primers isomkatefusdir and isomkate_rev from plasmid pRAF33. The second fragment was PCR amplified using primers isotetRfusrev and isotetRfus_dir using plasmid R100 as template, and contained *tetR*. The third fragment was generated by linearizing expression vector pBAD33 using Xba I digestion. Plasmid pRRG62 (fig. S1A, upper left side) was constructed by substituting the replication origin of pRRG54 (p15A) with the replication origin of plasmid pSEVA121 (RK2). This way, we constructed an expression vector for TetR$_{mkate2}$ with a lower plasmid copy number, which allowed us to control TetR expression more tightly. To generate plasmid pRRG62, TetR$_{mkate2}$ was PCR amplified from pRRG54 using primers pbadseva1 and pbadseva2. The resulting band was digested with Pac I and Spe I restriction endonucleases and inserted in pSEVA121 (*37*). Plasmid pRRG63 (fig. S1A) contains TetR$_{mkate2}$ and its target promoter pA::GFP transcriptional fusion. To generate this plasmid, pA::GFP was PCR amplified from plasmid pRRG13 using primers pua66terb1007 and ptetAgfpkm_revPacI. This PCR fragment was inserted into plasmid pRRG62 using Pac I and Hind III restriction endonucleases. This way, the bidirectional transcriptional terminator BBa_B1007 (http://parts.igem.org) was inserted, isolating TetR$_{mkate2}$ and pA::GFP cistrons. In plasmid pRRG74, TetR$_{mkate2}$ is expressed from promoter pR, while the pA::GFP fragment is located in the region occupied by pA::TetA in Tn*10*. Plasmid pRRG74 was generated by Gibson assembly, fusing three DNA fragments. The first one included *mkate2*, amplified using oligonucleotides pRRG74_mkatedir and pRRG74_mkaterev from plasmid pRAF22. The second one, containing the *gfp* gene, was amplified from pUA66 using primers pRRG74_GFPdir and pRRG74_GFPrev. Last, the third one contained the Tn*10* region that includes *tetR*, pR, and pA. It was amplified from plasmid R100 using primers pRRG74_ptetArev and pRRG74_TetRrev.

Strain generation
Strain RRG112 was generated by transforming plasmids pRRG13 (Km^r) and pRRG62 (Amp^r) into *E. coli* BW27783 by electroporation. Strains RRS113 and RRS129 were generated by transforming plasmids pRRG63 (Km^r, Amp^r) and pRRG74 (Amp^r), respectively, into *E. coli* BW27783 by electroporation. Strain RRS247 was generated by inserting the region comprising the *araC* to *km* genes (both included) from plasmid pRRG63 into *E. coli* chromosome. This way, strain RRS247 is the chromosomal counterpart of strain RRS113 (fig. S1A). The DNA fragment was PCR amplified from RRS113 using primers AraC_Wanner and Km_AraD_Wanner. These primers contained a homologous region to the *ara* operon such that the amplified fragment could be recombined into *E. coli* TB10 strain following the protocol described in (*38*). A P1 lysate was then prepared and transduced to strain BW27783 to yield strain RRS247.

Culture conditions
Unless otherwise stated, bacterial growth for DNA extraction and strain propagation was performed in LB, and cells were grown at 37°C, with orbital shaking and supplemented with appropriate antibiotic concentrations. Antibiotic concentrations used were as follows: ampicillin (Amp; 100 μg/ml), chloramphenicol (Cm; 25 μg/ml), and kanamycin (Km; 50 μg/ml). Arabinose induction for pBAD-regulated constructions used the concentrations shown in Supplementary Results and fig. S4, following the protocol described in (*39*).

DNA purification
Plasmid DNA was purified using the GeneJet Plasmid Miniprep Kit, following the vendor's instructions. Total DNA was extracted using Bio-Rad's InstaGene Matrix, following the vendor's instructions.

Growth rate determination
Growth rates were determined by measuring the absorbance in a Victor3 (PerkinElmer) microplate reader. Cells were grown in M9 medium supplemented with casamino acids [0.2% (w/v)] as nitrogen source and glycerol or glucose (0.5%) as carbon source. Cells were pregrown in flasks at 37°C overnight and then subjected to a 1:1000-fold dilution in fresh medium. A total of 150 μl of these diluted cultures were added to the wells of a 96-well microtiter plate (Deltalab). Absorbance values at 600 nm were taken every 7 min. These absorbance values were background subtracted and transformed into OD$_{600}$ (optical density at 600 nm) values by using a calibrating curve obtained with a Shimadzu UV-1603 spectrophotometer. Growth rates

(α) were obtained by fitting the growth curve between $OD_{600} = 0.1$ and $OD_{600} = 0.3$ to an exponential. Doubling times (τ) were obtained from growth rates as $\tau = \ln(2)/\alpha$. When inducers were added to the growth medium (either arabinose or Tc), pre-inoculums were supplemented with the same concentration of inducer to be tested.

Fluorescence microscopy
Cell cultures were pregrown overnight, starting from a 1:1000 dilution from a master glycerol stock. Cells were grown at 37°C in M9 medium (Fluka-Sigma M9 salts supplemented with 100 μM $CaCl_2$, 20 mM $MgSO_4$, 0.2% casamino acids, and 0.5% glucose or glycerol). Appropriate concentrations of arabinose/glucose/glycerol/Tc were added according to the experimental requirements. Overnight saturated cultures were diluted 1:1000 in the same medium and incubated at 37°C for 2 to 3 hours until they reached $OD_{600} = 0.1$ to 0.2. Thus, cells were grown for approximately 16 generations in the same growth medium before their analysis by fluorescence microscopy. A total of 2 μl of cells were placed onto agarose pads containing the same growth medium used for preimaging growth. Agarose pads were generated by stacking an adhesive frame (Frame-Seal Incubation Chamber, Bio-Rad) onto a microscope slide. In the cavity formed by the adhesive frame, a volume of 200 μl of hot M9 medium + 1.5% agarose was added. Another microscope slide was placed over the frame immediately after pouring M9 + agarose to obtain a uniform and leveled gel. M9 medium used to generate agar pads was supplemented with the appropriate arabinose/glucose/glycerol/Tc concentrations. Pads were allowed to cool down for 30 min at room temperature, and then, using a sterile scalpel, a square of about 0.25 cm^2 of the agarose gel was cut. The rest of the agarose pad was removed, and 2 μl of the appropriate culture was placed on top of the pad. The culture droplet was allowed to dry for approximately 5 min, and then, a coverslip was placed over the frame, sealing it carefully. Sealed pads were transferred to the slide holder of a Leica AF6500 inverted epifluorescence microscope, inside an environmental chamber that was kept at 37°C along the course of the experiment. Cells were allowed to adapt to the pad and temperature for 30 min before we started to image. Images were acquired with ×630 magnification using HCX PL S-APO 63× 1.3 oil objective. We acquired images in phase contrast and in the green and red fluorescence channels. Filters used for fluorescence images were 562/40-nm excitation and 641/75-nm emission for mKate2 and 482/18-nm excitation and 520/28-nm emission for GFP. A Leica EL6000 external light engine, equipped with a mercury vapor lamp (HXP Short Arc Lamp, Osram), was used for fluorescence excitation. All images were obtained using the excitation lamp at maximum power. Images were acquired using a 12-bit Andor iXon885 high-speed camera, without binning. For red fluorescence images, we used two exposure times (500 ms and 2 s) in all images taken. For the green fluorescence channel, variable exposure times were applied (10 ms, 100 ms, and 1 s). To avoid fluorescence bleaching from previous exposures, snapshots were taken at least four fields of view away from each other. Linearity of the fluorescence emission with exposure time was checked using a set of predefined fluorescence beads (Rainbow Fluorescent Particle Slide, Spherotech) (fig. S1B).

Image analysis
Images were acquired using LAS AF software (Leica) and exported to TIF format. All image analysis procedures were performed using Matlab (MathWorks). First, a flat-field correction was applied to compensate for field curvature. For this purpose, at least 10 empty field images were taken using the same microscope and camera configurations used later in the corresponding experiment. Images were then averaged, and a correcting matrix was generated. This correcting matrix was applied on a second set of empty field images to check that it produced a flat field (fig. S1B). This correcting matrix was then used on the experimental images to correct for field curvature. Cell segmentation was generated from phase images using MicrobeTracker (40). Algorithm parameters were fine-tuned to obtain the best segmentation mask possible. Manual curation was nevertheless necessary, so each frame was manually corrected to guarantee proper segmentation masks. From these segmentation masks, we extracted cell length, area, and fluorescence intensities in all relevant channels. Cell size was used as a proxy to check the uniformity of growth conditions. For this purpose, cell size histograms were generated for all frames. Frames that produced cell size histograms 1 SD outside the norm were discarded. Fluorescence shift with respect to phase images was checked by manually curating a set of segmentation masks and then comparing its resulting values to the original ones obtained without shift correction. Fluorescence values were background subtracted using MicrobeTracker algorithm (40). Fluorescence intensities were generated by normalizing fluorescence values by their corresponding cell area and exposure time. All fluorescence intensities are thus reported in arbitrary units/(ms × μm^2).

REFERENCES AND NOTES
1. H. C. Berg, E. M. Purcell, Physics of chemoreception. *Biophys. J.* **20**, 193–219 (1977).
2. I. Lestas, G. Vinnicombe, J. Paulsson, Fundamental limits on the suppression of molecular fluctuations. *Nature* **467**, 174–178 (2010).
3. W. Bialek, S. Setayeshgar, Physical limits to biochemical signaling. *Proc. Natl. Acad. Sci. U.S.A.* **102**, 10040–10045 (2005).
4. K. Kaizu, W. de Ronde, J. Paijmans, K. Takahashi, F. Tostevin, P. R. ten Wolde, The Berg-Purcell limit revisited. *Biophys. J.* **106**, 976–985 (2014).
5. A. Eldar, M. B. Elowitz, Functional roles for noise in genetic circuits. *Nature* **467**, 167–173 (2010).
6. P. R. ten Wolde, N. B. Becker, T. E. Ouldridge, A. Mugler, Fundamental limits to cellular sensing. *J. Stat. Phys.* **162**, 1395–1424 (2016).
7. R. Cheong, A. Rhee, C. J. Wang, I. Nemenman, A. Levchenko, Information transduction capacity of noisy biochemical signaling networks. *Science* **334**, 354–358 (2011).
8. J. Selimkhanov, B. Taylor, J. Yao, A. Pilko, J. Albeck, A. Hoffmann, L. Tsimring, R. Wollman, Accurate information transmission through dynamic biochemical signaling networks. *Science* **346**, 1370–1373 (2014).
9. A. S. Hansen, E. K. O'Shea, Limits on information transduction through amplitude and frequency regulation of transcription factor activity. *eLife* **4**, e06559 (2015).
10. G. Tkačik, C. G. Callan Jr., W. Bialek, Information flow and optimization in transcriptional regulation. *Proc. Natl. Acad. Sci. U.S.A.* **105**, 12265–12270 (2008).

11. S. Uda, T. H. Saito, T. Kudo, T. Kokaji, T. Tsuchiya, H. Kubota, Y. Komori, Y.-i. Ozaki, S. Kuroda, Robustness and compensation of information transmission of signaling pathways. *Science* **341**, 558–561 (2013).

12. C. G. Bowsher, P. S. Swain, Environmental sensing, information transfer, and cellular decision-making. *Curr. Opin. Biotechnol.* **28**, 149–155 (2014).

13. M. D. Brennan, R. Cheong, A. Levchenko, How information theory handles cell signaling and uncertainty. *Science* **338**, 334–335 (2012).

14. J. Estrada, F. Wong, A. DePace, J. Gunawardena, Information integration and energy expenditure in gene regulation. *Cell* **166**, 234–244 (2016).

15. B. Eckert, C. F. Beck, Overproduction of transposon Tn10-encoded tetracycline resistance protein results in cell-death and loss of membrane-potential. *J. Bacteriol.* **171**, 3557–3559 (1989).

16. D. I. Andersson, D. Hughes, Microbiological effects of sublethal levels of antibiotics. *Nat. Rev. Microbiol.* **12**, 465–478 (2014).

17. L. E. Ulrich, E. V. Koonin, I. B. Zhulin, One-component systems dominate signal transduction in prokaryotes. *Trends Microbiol.* **13**, 52–56 (2005).

18. D. Landgraf, B. Okumus, P. Chien, T. A. Baker, J. Paulsson, Segregation of molecules at cell division reveals native protein localization. *Nat. Methods* **9**, 480–482 (2012).

19. G. Tkačik, W. Bialek, Information Processing in Living Systems. *Annu. Rev. Condens. Matter Phys.* **7**, 89–117 (2016).

20. A. Khlebnikov, Ø. Risa, T. Skaug, T. A. Carrier, J. D. Keasling, Regulatable arabinose-inducible gene expression system with consistent control in all cells of a culture. *J. Bacteriol.* **182**, 7029–7034 (2000).

21. S. Tal, J. Paulsson, Evaluating quantitative methods for measuring plasmid copy numbers in single cells. *Plasmid* **67**, 167–173 (2012).

22. S. P. Strong, R. Koberle, R. R. d. van Steveninck, W. Bialek, Entropy and information in neural spike trains. *Phys. Rev. Lett.* **80**, 197–200 (1998).

23. L. Paninski, Estimation of entropy and mutual information. *Neural Comput.* **15**, 1191–1253 (2003).

24. G. Tkacik, A. M. Walczak, W. Bialek, Optimizing information flow in small genetic networks. III. A self-interacting gene. *Phys. Rev. E Stat. Nonlin. Soft Matter Phys.* **85**, 041903 (2012).

25. T. Taillefumier, N. S. Wingreen, Optimal census by quorum sensing. *PLOS Comput. Biol.* **11**, e1004238 (2015).

26. J. Paulsson, Summing up the noise in gene networks. *Nature* **427**, 415–418 (2004).

27. G. Tkacik, C. G. Callan Jr., W. Bialek, Information capacity of genetic regulatory elements. *Phys. Rev. E Stat. Nonlin. Soft Matter Phys.* **78**, 011910 (2008).

28. J. O. Dubuis, G. Tkačik, E. F. Wieschaus, T. Gregor, W. Bialek, Positional information, in bits. *Proc. Natl. Acad. Sci. U.S.A.* **110**, 16301–16308 (2013).

29. I. Meier, L. V. Wray, W. Hillen, Differential regulation of the Tn10-encoded tetracycline resistance genes tetA and tetR by the tandem tet operators O1 and O2. *EMBO J.* **7**, 567–572 (1988).

30. R. Wollman, Robustness, accuracy, and cell state heterogeneity in biological systems. *Curr. Opin. Syst. Biol.* **8**, 46–50 (2018).

31. R. Suderman, J. A. Bachman, A. Smith, P. K. Sorger, E. J. Deeds, Fundamental trade-offs between information flow in single cells and cellular populations. *Proc. Natl. Acad. Sci. U.S.A.* **114**, 5755–5760 (2017).

32. P. Mehta, S. Goyal, T. Long, B. L. Bassler, N. S. Wingreen, Information processing and signal integration in bacterial quorum sensing. *Mol. Syst. Biol.* **5**, 325 (2009).

33. N. A. Rossi, M. J. Dunlop, Customized regulation of diverse stress response genes by the multiple antibiotic resistance activator MarA. *PLOS Comput. Biol.* **13**, e1005310 (2017).

34. G. Tkačik, A. M. Walczak, W. Bialek, Optimizing information flow in small genetic networks. *Phys. Rev. E Stat. Nonlin. Soft Matter Phys.* **80**, 031920 (2009).

35. E. Gullberg, S. Cao, O. G. Berg, C. Ilbäck, L. Sandegren, D. Hughes, D. I. Andersson, Selection of resistant bacteria at very low antibiotic concentrations. *PLOS Pathog.* **7**, e1002158 (2011).

36. J. Davies, G. B. Spiegelman, G. Yim, The world of subinhibitory antibiotic concentrations. *Curr. Opin. Microbiol.* **9**, 445–453 (2006).

37. R. Silva-Rocha, E. Martínez-García, B. Calles, M. Chavarría, A. Arce-Rodríguez, A. de Las Heras, A. D. Páez-Espino, G. Durante-Rodríguez, J. Kim, P. I. Nikel, R. Platero, V. de Lorenzo, The Standard European Vector Architecture (SEVA): A coherent platform for the analysis and deployment of complex prokaryotic phenotypes. *Nucleic Acids Res.* **41**, D666–D675 (2013).

38. K. A. Datsenko, B. L. Wanner, One-step inactivation of chromosomal genes in *Escherichia coli* K-12 using PCR products. *Proc. Natl. Acad. Sci. U.S.A.* **97**, 6640–6645 (2000).

39. R. Fernandez-Lopez, I. Del Campo, R. Ruiz, V. Lanza, L. Vielva, F. de la Cruz, Numbers on the edges: A simplified and scalable method for quantifying the gene regulation function. *Bioessays* **32**, 346–355 (2010).

40. O. Sliusarenko, J. Heinritz, T. Emonet, C. Jacobs-Wagner, High-throughput, subpixel precision analysis of bacterial morphogenesis and intracellular spatio-temporal dynamics. *Mol. Microbiol.* **80**, 612–627 (2011).

Citation: R. Ruiz, F. de la Cruz, R. Fernandez-Lopez, Negative feedback increases information transmission, enabling bacteria to discriminate sublethal antibiotic concentrations. *Sci. Adv.* **4**, eaat5771 (2018).